

The critical pressure for microfiltration of oil-in-water emulsions using slotted-pore membranes

Tohid Darvishzadeh¹, Bishal Bhattarai², Nikolai V. Priezjev^{2,3}

¹*Department of Mechanical Engineering,*

Michigan State University, East Lansing, MI 48824

²*Department of Mechanical and Materials Engineering,*

Wright State University, Dayton, OH 45435 and

³*National Research University Higher School of Economics, Moscow 101000, Russia*

(Dated: March 4, 2022)

Abstract

The influence of geometrical parameters and fluid properties on the critical pressure of permeation of an oil micro-droplet into a slotted pore is studied numerically by solving the Navier-Stokes equations. We consider a long slotted pore, which is partially blocked by the oil droplet but allows a finite permeate flux. An analytical estimate of the critical permeation pressure is obtained from a force balance model that involves the drag force from the flow around the droplet and surface tension forces as well as the pressure variation inside the pore. It was found that numerical results for the critical pressure as a function of the oil-to-water viscosity ratio, surface tension coefficient, contact angle, and droplet radius agree well with theoretical predictions. Our results show that the critical permeation pressure depends linearly on the surface tension coefficient, while the critical pressure nearly saturates at sufficiently large values of the viscosity ratio or the droplet radius. These findings are important for an optimal design and enhanced performance of microfiltration systems with slotted pores.

Keywords: multiphase flows; microfiltration; emulsions; Volume of Fluid method; membrane fouling; slotted pore

I. INTRODUCTION

The efficient microfiltration of oil-in-water emulsions, that are commonly found in produced water from oil/gas recovery or as a byproduct of metal finishing processes, is important for protection of the aquatic environment and recovery of clean water [1, 2]. The advantages of the membrane filtration methods, as compared to sedimentation, dissolved gas flotation and centrifugation, include relatively low maintenance cost, mechanical stability and simple operating conditions [3–6]. The membrane separation process is based on rejection of non-wetting oil droplets that are larger than membrane pores, while at the same time allowing permeate flux, which is induced by the applied pressure across the membrane. However, the major practical challenge in achieving a high permeate flux is the membrane fouling [7]. Common antifouling strategies include crossflow filtration, physical or chemical cleaning, surface wettability modification, stabilization by surfactants, and electrostatic repulsion [8–13]. More recently, a multicontinuum approach for estimation of the permeation capacity of thin flat membranes with a broad distribution of pore openings was formulated for oil-water emulsions with different droplet sizes and then validated using the experimental data [14, 15].

At the microscopic level, the critical transmembrane pressure required for an oil droplet to permeate into a membrane pore can be deduced from the analysis of the Young-Laplace pressure across curved oil-water interfaces inside and above the pore [16]. In the absence of crossflow, a simple model for the critical pressure of permeation of an oil droplet into a circular pore was validated via detailed numerical simulations [17] and experimental measurements [16]. As an aside, an analytical expression for the critical permeation pressure in the case of a continuous oil film above a membrane surface with a pore of arbitrary cross-section was obtained and validated for rectangular and elliptical pores [17]. It was later shown that in the presence of crossflow along the membrane surface, the critical pressure increases due to the drag force generated by the shear flow around an oil droplet, and, at sufficiently high shear rates, the droplet above the pore breaks up into two segments [17–19]. The results of numerical simulations have demonstrated that the breakup capillary number and the increase in critical pressure due to crossflow are nearly independent of the contact angle but depend strongly on the oil-to-water viscosity ratio, surface tension, and drop-to-pore size ratio [18]. Recent experimental studies on crossflow microfiltration have shown that membrane fouling might involve several stages, namely, droplet attachment and

clustering, droplet deformation and coalescence [20] and that the critical flux decreases with salt concentration [21]. Using CFD modeling, it was also recently found that membrane fouling can be reduced by applying sufficiently large electric field, which results in the oil droplet detachment from the membrane surface [22].

One of the key factors for the efficient microfiltration of oil-in-water dispersions is the pore size and shape [23–27]. In particular, it was reported that, under similar operating conditions, the critical flux through a membrane with slotted pores is much higher than the flux through circular pore membranes [28]. This result can be intuitively understood from the fact that an oil droplet can only partially block a long slotted pore and thus allow a finite permeate flux, whereas a relatively large oil droplet can completely block a circular pore. It was later shown that the experimental data for rejection of oil droplets by slotted pore membranes are well described by theoretical predictions, assuming that a spherical droplet deforms into an ellipsoid inside the pore and taking into account the static and drag forces [29]. An improved rejection of oil droplets through the slotted pore membrane can also be achieved by imposing vibration that leads to shear-induced migration and an inertial lift of droplets from the membrane surface [30]. Despite significant progress, however, the exact physical mechanism of the droplet permeation into a slotted pore even at the initial filtration stage and in the absence of crossflow is not fully understood.

In this paper, we investigate the process of oil droplet permeation into a slotted pore under applied pressure using numerical simulations and the Volume of Fluid method to track the oil-water interface. The critical permeation pressure is first estimated theoretically using a force balance analysis of the capillary forces and the drag force from the flow around the droplet. It will be shown that theoretical predictions agree well with the numerically obtained critical pressure as a function of the oil-to-water viscosity ratio, the surface tension coefficient, the contact angle, and the droplet radius.

The remainder of the paper is organized as follows. In the next section, the numerical simulation method and governing equations are presented. The theoretical prediction for the critical permeation pressure based on the force balance arguments is given in Sec. III A, and the results of numerical simulations and comparison with analytical predictions are reported in Sec. III B. The brief summary of the results is provided in the last section.

II. NUMERICAL SIMULATIONS

The interaction of an oil droplet with the porous membrane surface was studied numerically by solving the Navier-Stokes equation, which is implemented in the commercial software ANSYS FLUENT [31]. In turn, the dynamics of an oil-water interfaces was tracked by the the Volume of Fluid (VOF) method, where computational cells contain information on the volume fraction of each phase [32]. More specifically, we considered an oil droplet at the entrance of a slotted pore and applied a pressure difference across the membrane, which induces a flow around the droplet, as shown schematically in Fig. 1. The numerical methodology for the problem of an oil droplet at a slotted pore is very similar to the numerical setup used in our previous papers, where the permeation, rejection and breakup of an oil droplet at a circular pore was investigated for a number of material parameters and various operating conditions [17, 18]. In particular, we performed test simulations to determine the appropriate domain size and grid resolution necessary to accurately capture the effects of interface curvature and flow around the droplet. It was found that the computational domain has to be at least 4 times the size of the droplet and that at least 20 mesh cells are required across the pore. As discussed below, we considered an infinitely long slotted pore by using a symmetry boundary condition, thus eliminating the finite size effects due to pore ends. The numerical values of the geometrical and material parameters are listed at the end of Sec. III A.

In the Volume of Fluid method [32], the oil-water interface is specified by the volume fraction α , which is coupled to the flow via the solution of the transport equation as follows:

$$\frac{\partial \alpha}{\partial t} + \nabla \cdot (\alpha \mathbf{V}) = 0, \quad (1)$$

where \mathbf{V} is the local velocity vector. The material properties near interfaces and in the bulk are averaged within each cell based on the volume fraction of each phase. For example, the averaged local density is obtained as follows:

$$\rho = \alpha \rho_2 + (1 - \alpha) \rho_1. \quad (2)$$

Next, the following momentum equation is solved numerically using the average fluid viscosity and density:

$$\frac{\partial}{\partial t}(\rho \mathbf{V}) + \nabla \cdot (\rho \mathbf{V} \mathbf{V}) = -\nabla p + \nabla \cdot [\mu(\nabla \mathbf{V} + \nabla \mathbf{V}^T)] + \rho \mathbf{g} + \mathbf{F}, \quad (3)$$

where \mathbf{V} is the velocity vector, \mathbf{g} is gravity, and \mathbf{F} is the local surface tension force at the curved interface, which is defined as:

$$\mathbf{F} = \sigma \frac{\rho \kappa \nabla \alpha}{\frac{1}{2}(\rho_1 + \rho_2)}, \quad (4)$$

where κ is the local curvature of the oil-water interface and σ is the surface tension coefficient. The local curvature, κ , is computed as follows:

$$\kappa = \frac{1}{|\mathbf{n}|} \left[\left(\frac{\mathbf{n}}{|\mathbf{n}|} \cdot \nabla \right) |\mathbf{n}| - (\nabla \cdot \mathbf{n}) \right], \quad (5)$$

where \mathbf{n} is the unit vector normal to the interface. Thus, the surface tension force given by Eq. (4) acts in the direction normal to the interface, and the magnitude of the force is larger for more curved interfaces [33]. Finally, the local orientation of the oil-water interface at the membrane or pore surfaces is determined by the static contact angle [34]. In practice, the unit vector normal to the interface at the solid surface is estimated as follows:

$$\mathbf{n}_i = \mathbf{n}_w \cos \theta + \mathbf{n}_t \sin \theta, \quad (6)$$

where the unit vectors \mathbf{n}_w and \mathbf{n}_t are normal to the wall and normal to the contact line, respectively. In our simulations, the contact angle is constant and it is strictly imposed at every surface of the membrane including the interior of the pore. Therefore, the contact angle hysteresis and dynamic contact angle effects were not considered in the present study. Also, the the gravitational and electrostatic forces were not included in the analysis.

The solver starts by generating a spherical droplet right above the pore entrance via a User-Defined-Function (UDF). Based on the droplet size and pore width, the UDF positions the droplet so that it barely touches the edges of the pore, thus facilitating attachment to the membrane surface and preventing upward migration at low transmembrane pressures. Another UDF subroutine applies a pressure-outlet boundary condition at the bottom of the pore, and the pressure difference across the simulation cell is increased from an initial value to a final value in a certain number of steps. During each step, the solver is iterated many times to reach a steady state. The position of the droplet interface inside the pore is actively monitored. With each increment of the transmembrane pressure up to a critical value, the droplet interface inside the pore is displaced away from the edges, while the whole droplet remains pinned at the pore entrance. At a particular step, a slight increase in the transmembrane pressure results in a dramatic acceleration of the droplet interface inside

the pore. This indicates the droplet permeation, and the critical pressure is calculated as the average value of the pressure jump at that particular step with an error bar of the step size. To compute the critical permeation pressure more accurately, the same process was repeated multiple times.

III. RESULTS

A. An estimate of the critical pressure based on the force balance

We consider an oil droplet residing at the entrance of a slotted pore shown schematically in Fig. 1. There are two main forces acting on the droplet; namely, the drag force from the viscous flow and the capillary forces. The competition between these forces determines the critical pressure required for permeation of the droplet inside the slotted pore. The permeation of the droplet involves a displacement of its interface into the pore, which, due to symmetry, moves along the centerline in the x direction (see Fig. 1). Therefore, only the x component of the forces needs to be included in the analysis and the other components are canceled due to symmetry. We define a control volume around the droplet as shown in Fig. 1. The viscous and pressure forces acting outside the control volume on two sides of the droplet (the side view) are counter-balanced by forces from pressure and surface tension forces from the surface of the membrane. These forces are expected to be much smaller than the forces acting on the control volume, since the shear stresses are smaller in the region outside the control volume.

First, the viscous flow around the droplet exerts a drag force, which is proportional to the viscosity of the continuous phase, viscosity ratio, average flow velocity, and droplet size. Since the flow field around the droplet gradually varies near the pore entrance, an exact analytical expression for the drag force is not available. However, due to the linearity of the flow at small Reynolds numbers, it can be assumed that the drag force is linearly proportional to the following parameters:

$$F_D \propto f(\lambda) \mu_w \bar{u} r_d, \quad (7)$$

where λ is the ratio of oil and water viscosities, μ_w is the viscosity of water, and \bar{u} is the average flow velocity around the droplet. The drag force is also a function of the viscosity

ratio via $f(\lambda)$. The form of such function is not readily known for our geometry. The flow accelerates at the entrance of the pore, while inside the pore and far away from the droplet, the velocity remains constant. This velocity is a result of the pressure gradient inside the pore. The pressure gradient induces a planar Hagen-Poiseuille flow inside the pore with a parabolic velocity profile. The average flow velocity in the pore is thus proportional to the following combination:

$$\bar{u} \propto \frac{W_p^2 |\Delta P|}{\mu_w L_p}, \quad (8)$$

where L_p is the length of the pore (see Fig. 1) and ΔP is the difference in static pressure from the bottom of the pore to the top of the channel. It is the critical value of this pressure that determines the critical permeation condition for the oil droplet.

After substituting the average velocity into Eq. (7), one can obtain the following equation for the drag force in terms of the pressure gradient along the pore:

$$F_D \propto \frac{f(\lambda) W_p^2 |\Delta P| r_d}{L_p}. \quad (9)$$

This force is counter-balanced by the capillary forces. Since the droplet permeation due to the transmembrane pressure is initiated by the displacement of the interface along the vertical direction, only the component of forces along the vertical (x) direction needs to be considered. Forces in other directions cancel each other due to symmetry. Figure 1 shows the control volume and the surface tension forces acting on the droplet. Note that the surface tension forces act in the tangential directions at the intersection of the dashed rectangular control volume and the droplet surface. The x component of the first force is estimated $F_{1_x} \approx 4 r_d \sigma \cos \beta_1$ and the second force acting on the droplet inside the channel is $F_{2_x} \approx 4 r_d \sigma \cos \beta_2$. The parameter σ is the surface tension coefficient between oil and water.

By definition, the angle $\beta_1 = 180^\circ - \theta$, where θ is the contact angle measured in oil, while the angle β_2 can be approximated as $\cos \beta_2 \approx \frac{W_p}{2 r_d}$. The model assumes that the retentive capillary force is a result of the competition between the capillary forces from two curved interfaces. If the droplet size is much larger than the pore width, then β_2 is close to 90° and the dominant capillary force will be at the oil-water interface inside the pore.

The summation of the two forces along the x direction yields:

$$F_{\sigma_x} \approx 2 \sigma W_p \left(\frac{2 r_d \cos \beta_1}{W_p} - 1 \right). \quad (10)$$

At the critical permeation pressure, the forces in Eq. (9) and Eq. (10) should be equal, *i.e.*, $F_D = F_{\sigma_x}$. Rearranging the terms gives:

$$\Delta P = K \frac{\sigma (2 r_d \cos \beta_1 / W_p - 1) L_p}{f(\lambda) W_p r_d}, \quad (11)$$

where K is the constant of proportionality. This expression, however, does not account for the pressure variation inside the pore. In the case of viscous flow inside the pore with no-slip boundary conditions (Hagen-Poiseuille flow), the pressure decreases linearly along the pore length, as shown for example in Fig. 2.

As will be shown in Sec. III B, sufficiently large transmembrane pressure results in the deformation of the oil droplet at the pore entrance. For sub-critical transmembrane pressures (below the critical value), the droplet remains at the pore entrance but it will be deformed by permeating incrementally inside the pore as the transmembrane pressure increases. Therefore, the surface of the droplet inside the pore is exposed to a pressure already reduced due to the linear pressure drop inside the pore, as shown in Fig. 2. This pressure is proportional to the droplet size, since larger droplets penetrate deeper inside the pore at sub-critical conditions. Therefore, the extra term for pressure can be approximated as $-\frac{r_d}{L_p} \Delta P$. Adding this term to the right-hand side of Eq. (11) gives:

$$\Delta P = K \frac{\sigma (2 r_d \cos \beta_1 / W_p - 1) L_p}{f(\lambda) W_p r_d} - \frac{r_d}{L_p} \Delta P. \quad (12)$$

Rearranging Eq. (12) and assuming $\Delta P = P_{cr}$, gives the following relation for the critical pressure of permeation of a droplet into an infinitely long slotted pore:

$$P_{cr} = K \frac{\sigma (2 r_d \cos \beta_1 / W_p - 1) L_p}{f(\lambda) W_p r_d (1 + r_d / L_p)}. \quad (13)$$

In the next section, we investigate the influence of oil-to-water viscosity ratio, surface tension, contact angle, and droplet size on the critical pressure of permeation using numerical simulations and compare the numerical results with the predictions of Eq. (13). Throughout the paper, the following values are used, unless explicitly noted otherwise: $r_d = 2 \mu\text{m}$, $W_p = 1 \mu\text{m}$, $L_p = 5 \mu\text{m}$, $\lambda = 1$, $\theta = 135^\circ$, and $\sigma = 19.1 \text{ mN/m}$.

B. Effect of physiochemical parameters on the critical pressure of permeation

In this section, the numerical simulations of an oil droplet permeating into an infinitely long slotted pore are performed (using the computational methods described in Sec. II)

and the results are compared to the theoretical model for the critical permeation pressure, Eq. (13), presented in Sec. III A.

In our computational setup, we have chosen a pore geometry that most closely resembles a slotted pore with a very large cross-sectional aspect ratio. More specifically, the pore is modeled as a slit with an infinite aspect ratio (which is implemented numerically by using the symmetry boundary conditions). This ensures that the oil droplet is unaffected by the finite size effects and, possibly, by other droplets on the same pore. The pore is assumed to be a perfectly rectangular cuboid with sharp edges. The value of the droplet radius in our simulations is the radius of a spherical droplet before depositing on the surface of the membrane. The radius of the droplet after depositing at the pore entrance, which is used in deriving the critical pressure given by Eq. (13), is only slightly different from the initial droplet radius and it is mainly dependent on the contact angle.

Figure 3 shows the flow streamlines as well as pressure distribution inside the pore and around the droplet at the initial stage of permeation. It can be seen that the pressure inside the droplet is higher than the outside pressure due to capillary forces. In addition, the flow inside the droplet undergoes a circulation caused by the shear stresses that are applied by the flow at the interface. As evident from Fig. 3, the streamlines begin at the top of the channel, continue across the pore and exit at the bottom of the pore. Notice that the flow is curved around the droplet, and the pressure distribution below the droplet deviates from the linear profile. As the Reynolds number is small, the flow is laminar and it remains attached to the droplet surface.

Figure 4 illustrates the shape evolution of the oil droplet inside the slotted pore. In our setup, the transmembrane pressure is initially set to a sub-critical value and then gradually increased up to the critical pressure. In the sub-critical regime, the oil droplet remains at the pore entrance and its lower part partially penetrates into the pore. When the pressure is increased up to the critical value, the permeation process accelerates drastically. At first, the lower part of the droplet starts stretching inside the pore, while the upper part remains temporarily pinned. Next, the droplet permeation is accelerated as the bottom of the droplet inside the pore experiences increasingly lower pressure as compared to the top of the droplet inside the channel (see Fig. 2). Eventually, the whole droplet enters the pore and deforms into an oblate disc with the major axis oriented along the flow direction. This stretching

is mainly caused by the linear pressure gradient inside the pore, as shown in Fig. 2. Once the droplet is completely inside the pore, the permeation proceeds very quickly. Finally, the droplet reaches the bottom of the pore and exits from it.

The effect of the oil-to-water viscosity ratio on the critical pressure of permeation of an oil droplet into a slotted pore is shown in Fig. 5. The results of numerical simulations (indicated by square symbols in Fig. 5) demonstrate that the critical pressure decreases monotonically with increasing viscosity ratio. This is because a larger viscosity ratio results in higher shear stress on the droplet, which in turn leads to larger deformation and consequently permeation at lower transmembrane pressures. In our analysis of the critical pressure, Eq. (13), the function $f(\lambda)$ is assumed to be same as for a spherical droplet in uniform viscous flow and it is given by [35]:

$$f(\lambda) = \frac{3\lambda + 2}{\lambda + 1}. \quad (14)$$

Furthermore, the proportionality constant in Eq. (13) was chosen to fit the numerical value of P_{cr} at $\lambda = 1$. Thus, the solid curve in Fig. 5 represents the theoretical prediction of Eq. (13). It can be seen that there is a good agreement between the theoretical prediction and the numerical results, especially for larger values of the viscosity ratio. With further increasing viscosity ratio, $f(\lambda) \approx 3$ and the critical pressure approaches an asymptotic value, as predicted by Eq. (13). The critical pressure decreases by about 15% from $\lambda = 1$ to $\lambda = 32$. Therefore, it can be concluded that the critical permeation pressure is a relatively weak function of the viscosity ratio as compared to other parameters such as the surface tension coefficient (discussed below).

We next consider the influence of surface tension on the critical pressure of permeation of an oil droplet deposited on a slotted pore. The numerical results and theoretical prediction of Eq. (13) are reported in Fig. 6. Similar to the case of the viscosity ratio, the proportionality coefficient in Eq. (13) was gauged at the numerical value of P_{cr} at $\sigma = 19.1$ mN/m. As is evident, the critical pressure is a linear function of the surface tension coefficient, implying that droplets with higher surface tension require higher transmembrane pressures to enter the pore. The excellent agreement between numerical results and analytical predictions also confirms the linearity of surface tension effect in the force balance analysis presented in Sec. III A. The fact that the extended theoretical line passes through zero critical pressure demonstrates that surface tension is one of the main factors that determine the permeation

of the oil phase through porous filters.

Figure 7 shows the critical pressure of permeation as a function of the factor $-\cos\theta$. To remind, θ is the contact angle measured in oil and it is related to the angle $\beta_1 = 180^\circ - \theta$ used in Eq. (13) and shown in Fig. 1. The theoretical line is fitted to the numerical data using Eq. (13) at the contact angle $\theta = 135^\circ$, which corresponds to $-\cos\theta = 0.707$, similar to the cases of viscosity ratio and surface tension. As seen in Fig. 7, the theoretical predictions agree well with numerical results, indicating a nearly linear dependence of the critical pressure on $-\cos\theta$. As discussed above, permeation of the droplet into the pore results in an increase in the effective surface area between oil and the pore wall (see Fig. 4). Thus, with increasing contact angle, the surface energy between the oil phase and the pore surface increases, and, as a result, the critical transmembrane pressure becomes higher.

Furthermore, it can be inferred from Eq. (13) that the critical permeation pressure becomes negative if $\cos\beta_1 < W_p/2r_d$. This also implies that at the contact angle of 90° , the droplet will permeate into the pore even at zero transmembrane pressure. Therefore, there should be a minimum contact angle, above which the droplet will remain at the membrane surface when there is no transmembrane pressure applied. This critical contact angle can be readily estimated from Eq. (13) by equating the right-hand side to zero and using the definition $\beta_1 = 180^\circ - \theta$ to obtain:

$$\theta_{cr} = 180^\circ - \arccos\left(\frac{W_p}{2r_d}\right). \quad (15)$$

Plugging in our standard parameters $r_d = 2\mu\text{m}$ and $W_p = 1\mu\text{m}$ into Eq. (15) results in the critical contact angle of $\theta = 104.5^\circ$. This value is confirmed by numerical simulations to be $\theta = 103^\circ$, as shown in Fig. 7 by the square symbol at $-\cos\theta = 0.23$.

The size of the oil droplet has two effects on the balance of forces that determine the critical pressure of permeation. First, as predicted by Eq. (9), larger droplets experience higher drag force from the flow passing around its surface. Second, as discussed in Sec. III A, larger droplets tend to penetrate deeper into the pore even at sub-critical pressures. This results in an extra pressure gradient in the flow direction and, thus, indirectly contributes to the drag force as well [see Eq. (12)]. The results of numerical simulations as well as the theoretical prediction of Eq. (13) are summarized in Fig. 8. The theoretical curve is fitted to P_{cr} at $r_d = 2\mu\text{m}$ using Eq. (13), similar to the previous cases. One can observe a good agreement between the theoretical curve and the numerical data. The results in

Fig. 8 show that the critical pressure of permeation increases with the droplet radius up to a certain value. In particular, it can be seen that a droplet with the radius of about $2.4 \mu\text{m}$ requires the highest permeation pressure. This trend can be understood from the fact that the drag force due to the extra pressure gradient is smaller than the surface tension forces, and, therefore, as the droplet size increases, so does the transmembrane pressure needed for the droplet permeation. However, for droplets larger than a certain size, the drag force caused by the extra pressure gradient becomes relatively large, and, as a result, the critical permeation pressure becomes only weakly dependent on the droplet size (see Fig. 8).

IV. CONCLUSIONS

In summary, we investigated numerically the problem of an oil droplet permeation into a slotted pore under the applied transmembrane pressure. This situation is relevant to filtration of dilute oil-in-water emulsions, where the interaction between different droplets is not important and a single oil droplet blocks only a part of the slotted pore, thus allowing a finite permeate flux. More specifically, we considered an infinitely long slotted pore with sharp edges and parallel, nonwetting interior walls. The critical permeation pressure was first estimated theoretically by considering a difference between a drag force due to flow around a droplet and capillary forces due to curved oil-water interfaces, and taking into account a finite pressure variation inside the pore. The results of numerical simulations demonstrated that the critical pressure as a function of the oil-water viscosity ratio, surface tension, contact angle and droplet size agree well with theoretical predictions. In addition, an estimate of the critical contact angle, required for the permeation at zero applied pressure, was obtained and verified numerically. The simulation results also suggest that above a certain droplet size, the critical permeation pressure is only weakly dependent on the droplet radius.

Altogether, the numerical analysis of the droplet dynamics at the pore entrance and the theoretical prediction for the critical permeation pressure might be useful for development of efficient microfiltration systems. For example, by choosing an appropriate pressure across a slotted pore membrane, a dilute monodisperse oil-water emulsion that consists of two different dispersed fluids can be separated based on the viscosity ratio difference, thus allowing only one of the dispersed fluids to permeate. It is important to reiterate, however, that the key parameters that strongly influence the critical permeation pressure include the contact

angle, surface tension, and drop-to-pore ratio.

Acknowledgments

Financial support from the National Science Foundation (CNS-1531923 and CBET-1033662) and the Michigan State University Foundation (Strategic Partnership Grant 71-1624) is gratefully acknowledged. The article was prepared within the framework of the Basic Research Program at the National Research University Higher School of Economics (HSE) and supported within the framework of a subsidy by the Russian Academic Excellence Project ‘5-100’. Computational work in support of this research was performed at Michigan State University and Wright State University Computing Facilities and the Ohio Supercomputer Center.

-
- [1] S. Huang, R. H. A. Ras, and X. Tian, Antifouling membranes for oily wastewater treatment: Interplay between wetting and membrane fouling, *Curr. Opin. Colloid Interface Sci.* **36**, 90 (2018).
 - [2] X. Zhu, A. Dudchenko, X. Gu, and D. Jassby, Surfactant-stabilized oil separation from water using ultrafiltration and nanofiltration, *J. Membr. Sci.* **529**, 159 (2017).
 - [3] Y. Zhu, D. Wang, L. Jiang, and J. Jin, Recent progress in developing advanced membranes for emulsified oil/water separation, *NPG Asia Materials* **6**, 101 (2014).
 - [4] Q. Chang, J. Zhou, Y. Wang, J. Liang, X. Zhang, S. Cerneaux, X. Wang, Z. Zhu, and Y. Dong, Application of ceramic microfiltration membrane modified by nano-TiO₂ coating in separation of a stable oil-in-water emulsion, *J. Membr. Sci.* **456**, 128 (2014).
 - [5] C. Wang, C. Xiao, Q. Huang, and J. Pan, A study on structure and properties of poly(p-phenylene terephthamide) hybrid porous membranes, *J. Membr. Sci.* **474**, 132 (2015).
 - [6] G. Mustafa, K. Wyns, A. Buekenhoudt, and V. Meynen, Antifouling grafting of ceramic membranes validated in a variety of challenging wastewaters, *Water Research* **104**, 242 (2016).
 - [7] L. Song, Flux decline in crossflow microfiltration and ultrafiltration: Mechanisms and modeling of membrane fouling, *J. Membr. Sci.* **139**, 183 (1998).
 - [8] D. Lu, T. Zhang, and J. Ma, Ceramic membrane fouling during ultrafiltration of oil/water

- emulsions: Roles played by stabilization surfactants of oil droplets, *Environ. Sci. Technol.* **49**, 4235 (2015).
- [9] V. Carpintero-Tepole, E. Brito-de la Fuente, and B. Torrestiana-Sanchez, Microfiltration of oil in water (O/W) emulsions: Effect of membrane microstructure and surface properties, *Chem. Eng. Res. Des.* **126**, 286 (2017).
- [10] Z. He, D. J. Miller, S. Kasemset, D. R. Paul, and B. D. Freeman, The effect of permeate flux on membrane fouling during microfiltration of oily water, *J. Membr. Sci.* **525**, 25 (2017).
- [11] G. Fux and G. Z. Ramon, Microscale dynamics of oil droplets at a membrane surface: Deformation, reversibility, and implications for fouling, *Environ. Sci. Technol.* **51**, 13842 (2017).
- [12] M. S. Islam, J. R. McCutcheon, M. S. Rahaman, A high flux polyvinyl acetate-coated electrospun nylon 6/SiO₂ composite microfiltration membrane for the separation of oil-in-water emulsion with improved antifouling performance, *J. Membr. Sci.* **537**, 297 (2017).
- [13] G. Yi, S. Chen, X. Quan, G. Wei, X. Fan, H. Yu, Enhanced separation performance of carbon nanotube-polyvinyl alcohol composite membranes for emulsified oily wastewater treatment under electrical assistance, *Sep. Purif. Technol.* **197**, 107 (2018).
- [14] A. Salama, M. Zoubeik, and A. Henni, A multicontinuum approach for the problem of filtration of oily water systems across thin flat membranes: I. The framework, *AIChE Journal* **63**, 4604 (2017).
- [15] A. Salama, M. Zoubeik, and A. Henni, A multicontinuum approach for the problem of filtration of oily-water systems across thin flat membranes: II. Validation and examples, *AIChE Journal* **64**, 1095 (2018).
- [16] F. F. Nazzal and M. R. Wiesner, Microfiltration of oil-in-water emulsions, *Water Environ. Res.* **68**, 1187 (1996).
- [17] T. Darvishzadeh and N. V. Priezjev, Effects of crossflow velocity and transmembrane pressure on microfiltration of oil-in-water emulsions, *J. Membr. Sci.* **423-424**, 468 (2012).
- [18] T. Darvishzadeh, V. V. Tarabara, and N. V. Priezjev, Oil droplet behavior at a pore entrance in the presence of crossflow: Implications for microfiltration of oil-water dispersions, *J. Membr. Sci.* **447**, 442 (2013).
- [19] M. A. Monfared, N. Kasiri, and T. Mohammadi, Microscopic modeling of critical pressure of permeation in oily waste water treatment via membrane filtration, *RSC Adv.* **6**, 71744 (2016).
- [20] E. N. Tummons, V. V. Tarabara, J. W. Chew, and A. G. Fane, Behavior of oil droplets at

- the membrane surface during crossflow microfiltration of oil-water emulsions, *J. Membr. Sci.* **500**, 211 (2016).
- [21] H. J. Tanudjaja, V. V. Tarabara, A. G. Fane, and J. W. Chew, Effect of cross-flow velocity, oil concentration and salinity on the critical flux of an oil-in-water emulsion in microfiltration, *J. Membr. Sci.* **530**, 11 (2017).
- [22] M. A. Monfared, N. Kasiri, and T. Mohammadi, A CFD model for prediction of critical electric potential preventing membrane fouling in oily waste water treatment, *J. Membr. Sci.* **539**, 320 (2017).
- [23] P. Apel, Track etching technique in membrane technology, *Radiation Measurements* **34**, 559 (2001).
- [24] R. Ziel, A. Haus, and A. Tulke, Quantification of the pore size distribution (porosity profiles) in microfiltration membranes by SEM, TEM and computer image analysis, *J. Membr. Sci.* **323**, 241 (2008).
- [25] A. Ullah, R. G. Holdich, M. Naeem, and V. M. Starov, Microfiltration of deforming oil droplets on a slotted pore membrane and sustainable flux rates, *J. Membr. Sci.* **382**, 271 (2011).
- [26] F. Fan, L. Wang, W. Jiang, B. Chen, and H. Liu, A novel polyethylene microfiltration membrane with highly permeable ordered ‘wine bottle’ shaped through-pore structure fabricated via imprint and thermal field induction, *J. Phys. D: Appl. Phys.* **49**, 125501 (2016).
- [27] E. Benet and F. J. Vernerey, Mechanics and stability of vesicles and droplets in confined spaces, *Phys. Rev. E* **94**, 062613 (2016).
- [28] A. J. Bromley, R. G. Holdich, and I. W. Cumming, Particulate fouling of surface microfilters with slotted and circular pore geometry, *J. Membr. Sci.* **196**, 27 (2002).
- [29] A. Ullah, R. G. Holdich, M. Naeem, and V. M. Starov, Stability and deformation of oil droplets during microfiltration on a slotted pore membrane, *J. Membr. Sci.* **401-402**, 118 (2012).
- [30] A. Ullah, R. G. Holdich, M. Naeem, and V. M. Starov, Shear enhanced microfiltration and rejection of crude oil drops through a slotted pore membrane including migration velocities, *J. Membr. Sci.* **421-422**, 69 (2012).
- [31] Fluent, Inc., 2003. FLUENT 6.1 Users Guide.
- [32] C. W. Hirt and B. D. Nichols, Volume of Fluid (VOF) method for the dynamics of free boundaries, *J. Comput. Phys.* **39**, 201 (1981).
- [33] D. Gerlach, G. Tomar, G. Biswas, and F. Durst, Comparison of volume-of-fluid methods for

- surface tension-dominant two-phase flows, *Int. J. Heat Mass Transfer* **49**, 740 (2006).
- [34] J. U. Brackbill, D. B. Kothe, and C. Zemach, A continuum method for modeling surface tension, *J. Comp. Phys.* **100**, 335 (1992).
- [35] E. Loth, Quasi-steady shape and drag of deformable bubbles and drops, *Int. J. Multiphas. Flow* **34**, 523 (2008).

Figures

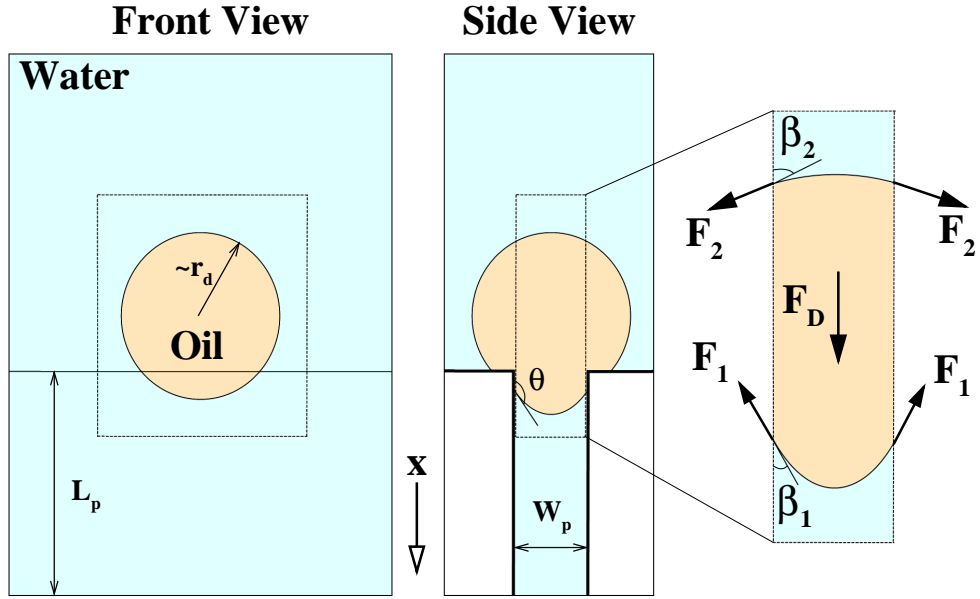


FIG. 1: (Color online) A schematic illustration of the oil droplet residing at the entrance of a slotted pore. The parameters L_p and W_p denote the length and width of the pore. The control volume is indicated by the dashed rectangles. An enlarged view of the control volume on the right-hand side shows the surface tension and drag forces as well as the local contact angles.

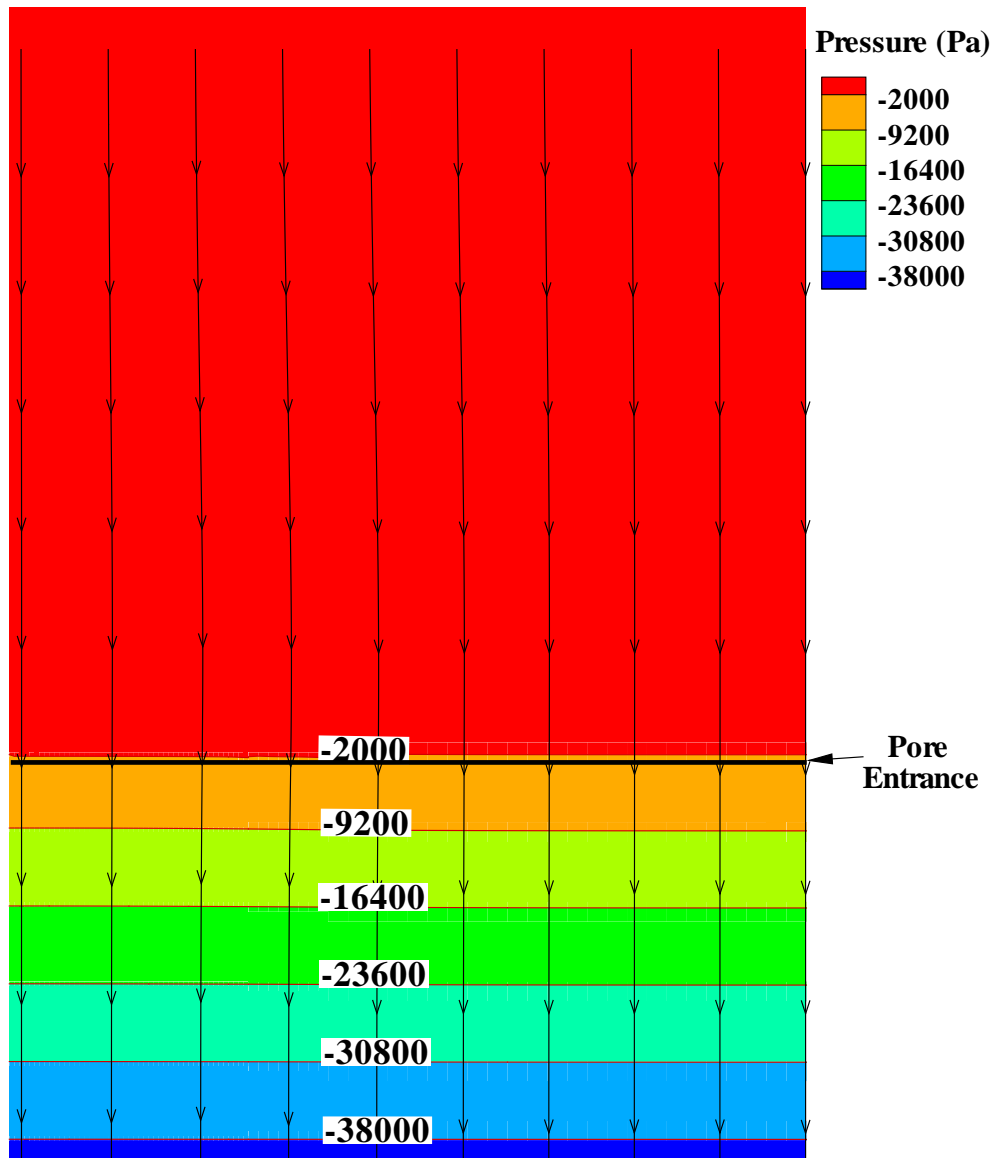


FIG. 2: (Color online) The pressure contours and streamlines along the plane that crosses the simulation domain and the slotted pore. The transmembrane pressure is 40 kPa. In the absence of an oil droplet, the flow across the pore is uniform. Notice that pressure along the streamlines varies linearly inside the pore.

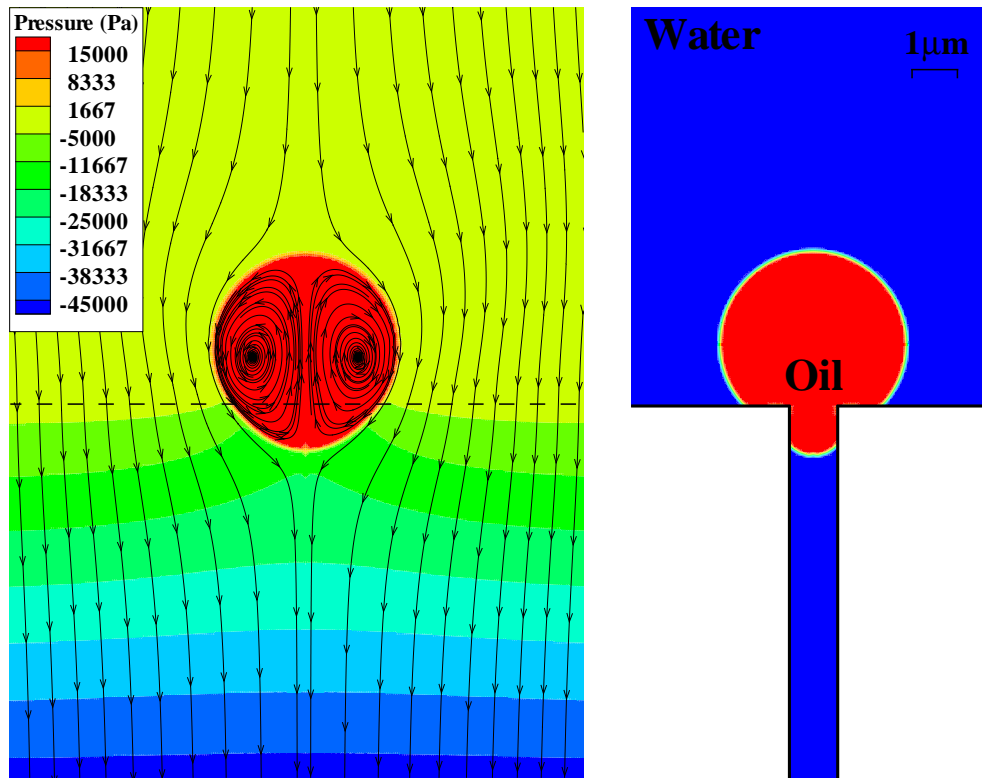


FIG. 3: (Color online) The left panel shows the distribution of pressure and flow streamlines at the transmembrane pressure of 45 kPa (front view) and the right panel displays the oil droplet at the entrance of the slotted pore (side view). The horizontal dashed line on the left panel indicates the pore entrance.

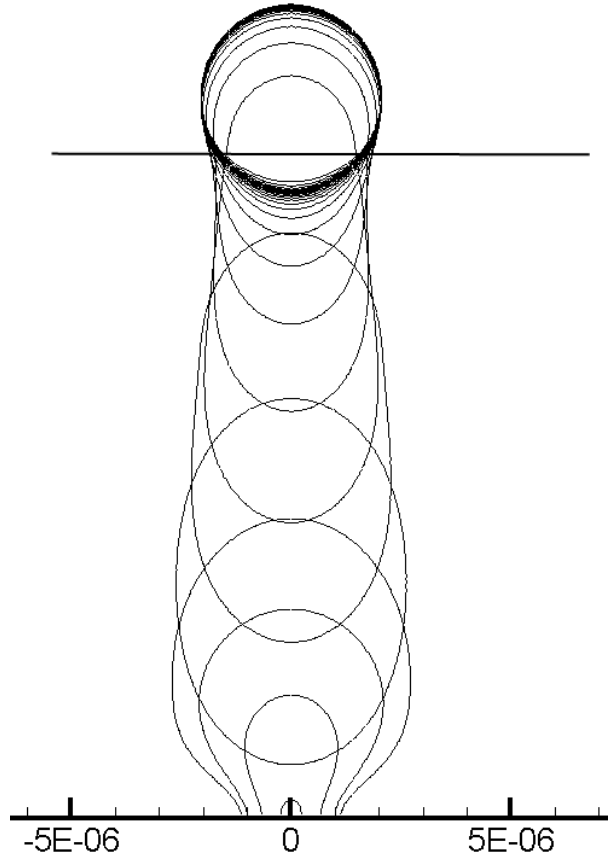


FIG. 4: The time sequence of the shape profiles inside the slotted pore illustrating the droplet permeation process (see text for details). The droplet radius is $r_d = 2 \mu\text{m}$.

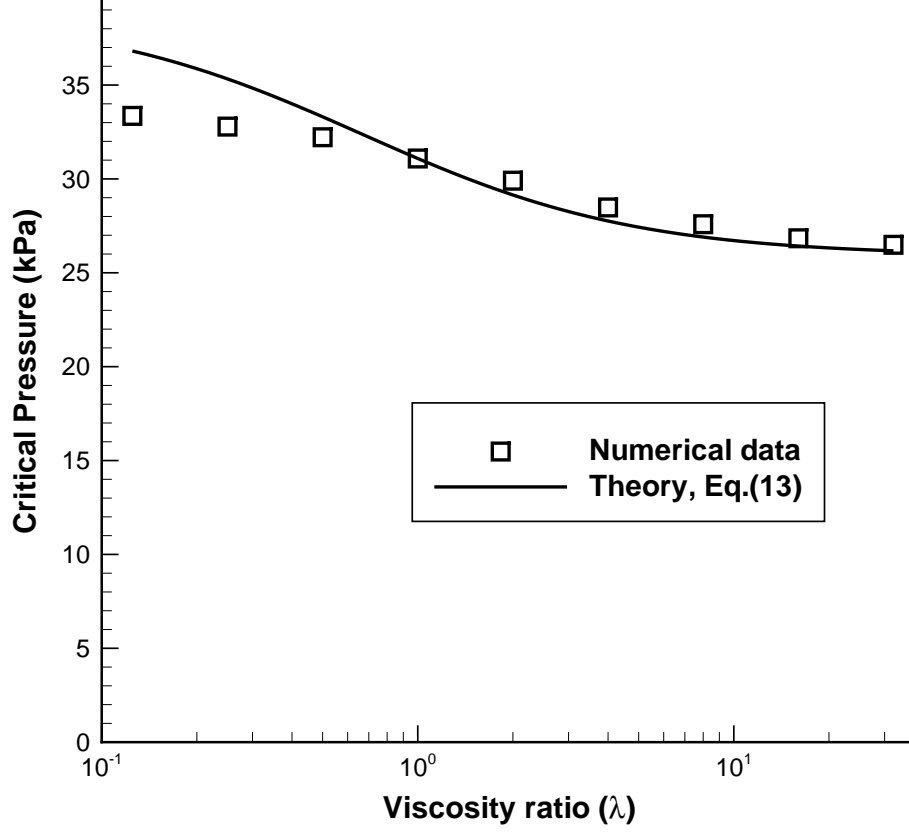


FIG. 5: The dependence of the critical permeation pressure as a function of the oil-to-water viscosity ratio, λ . Square symbols denote the numerical results and the solid line is the prediction of Eq. (13). The droplet radius is $r_d = 2 \mu\text{m}$, the surface tension coefficient is $\sigma = 19.1 \text{ mN/m}$, the contact angle is $\theta = 135^\circ$, and the slotted pore dimensions are $W_p = 1 \mu\text{m}$ and $L_p = 5 \mu\text{m}$.

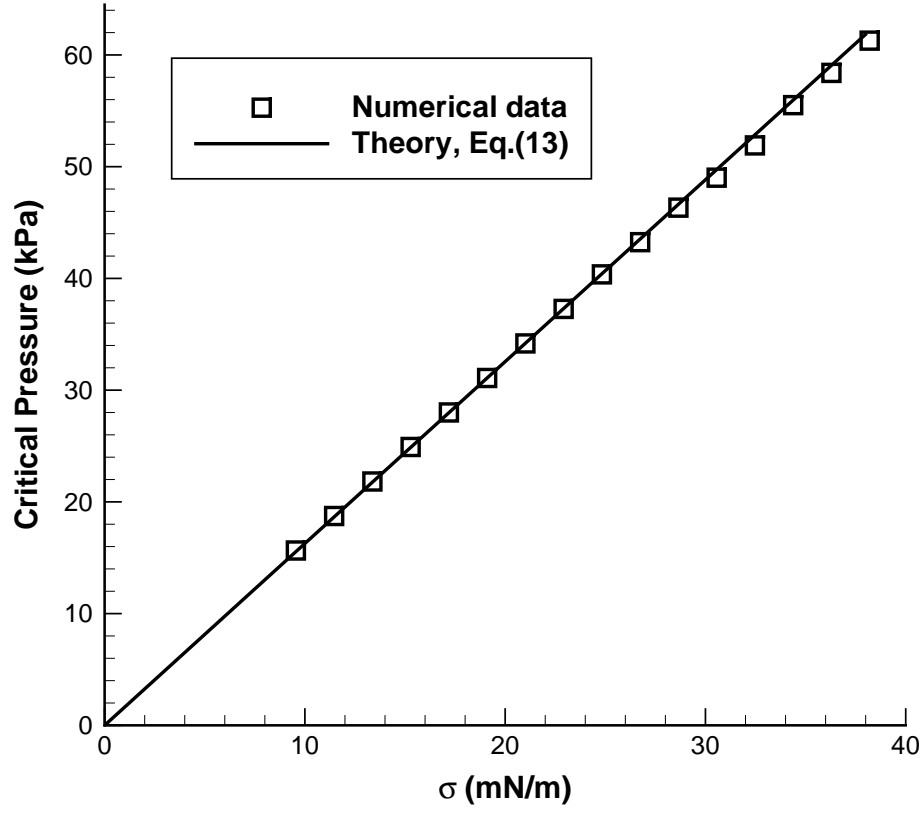


FIG. 6: The critical pressure of permeation of an oil droplet into a slotted pore as a function of the surface tension coefficient. The numerical results are indicated by symbols and the theoretical prediction of Eq. (13) is denoted by the solid line.

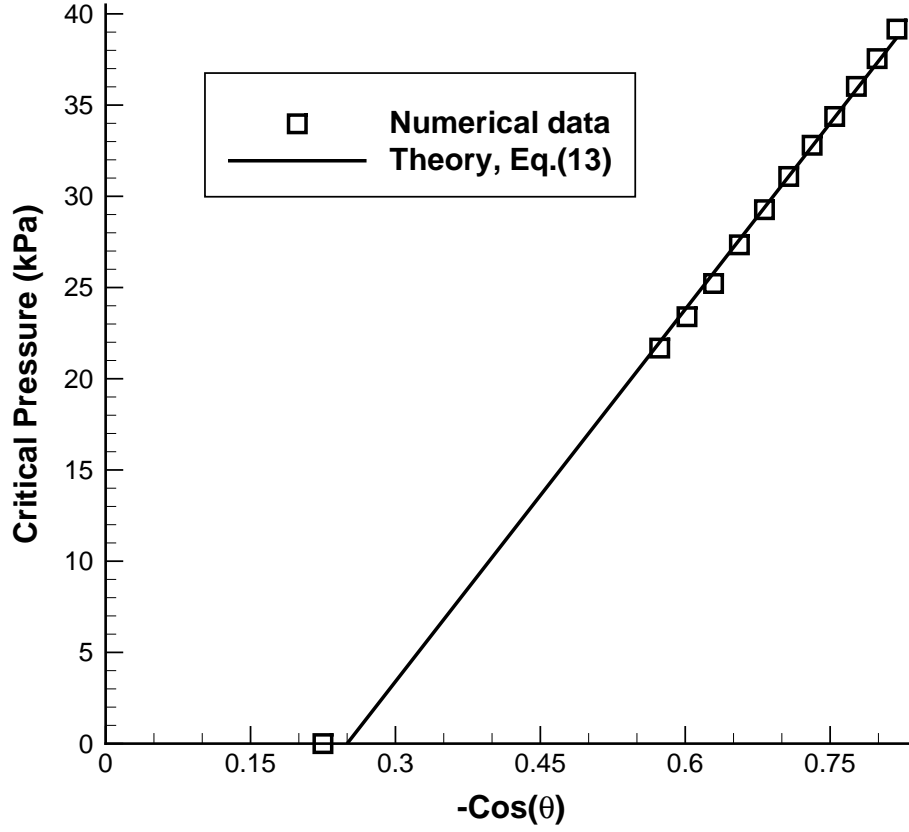


FIG. 7: The variation of the critical permeation pressure versus $-\cos\theta$. The numerical results and analytical prediction of Eq. (13) are indicated by symbols and the solid line, respectively. The square symbol at $-\cos\theta = 0.23$ denotes the numerical value of the critical contact angle when $P_{cr} = 0$.

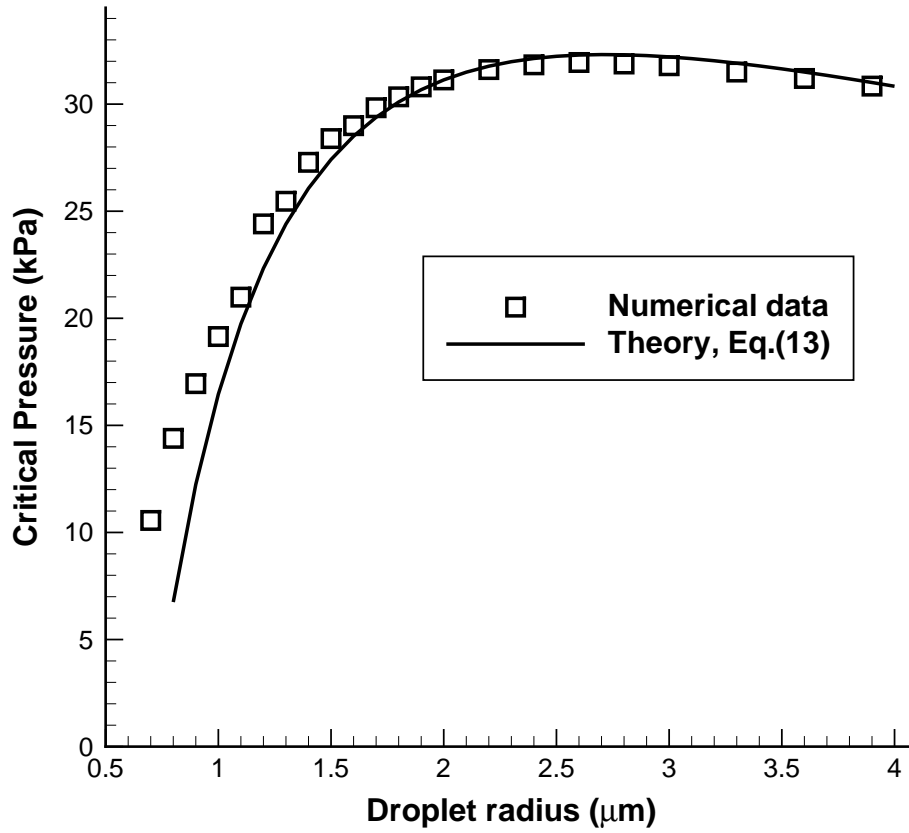


FIG. 8: The critical permeation pressure as a function of the droplet radius. The simulation results are denoted by square symbols, while the theoretical prediction of Eq. (13) is indicated by the solid curve.